Electronic Supplementary Material (ESI) for Nanoscale.


# Nanoparticle Localization in Blood Vessels: Dependence on Fluid Shear Stress, Flow Disturbances, and Flow-Induced Changes in Endothelial Physiology

*M. Juliana Gomez-Garcia, Amber L. Doiron, Robyn R. M. Steele, Hagar I. Labouta, Bahareh Vafadar, Robert D. Shepherd, Ian D. Gates, David T. Cramb, Sarah J. Childs, and Kristina D. Rinker** (kdrinker@ucalgary.ca)

**Supplementary Information**

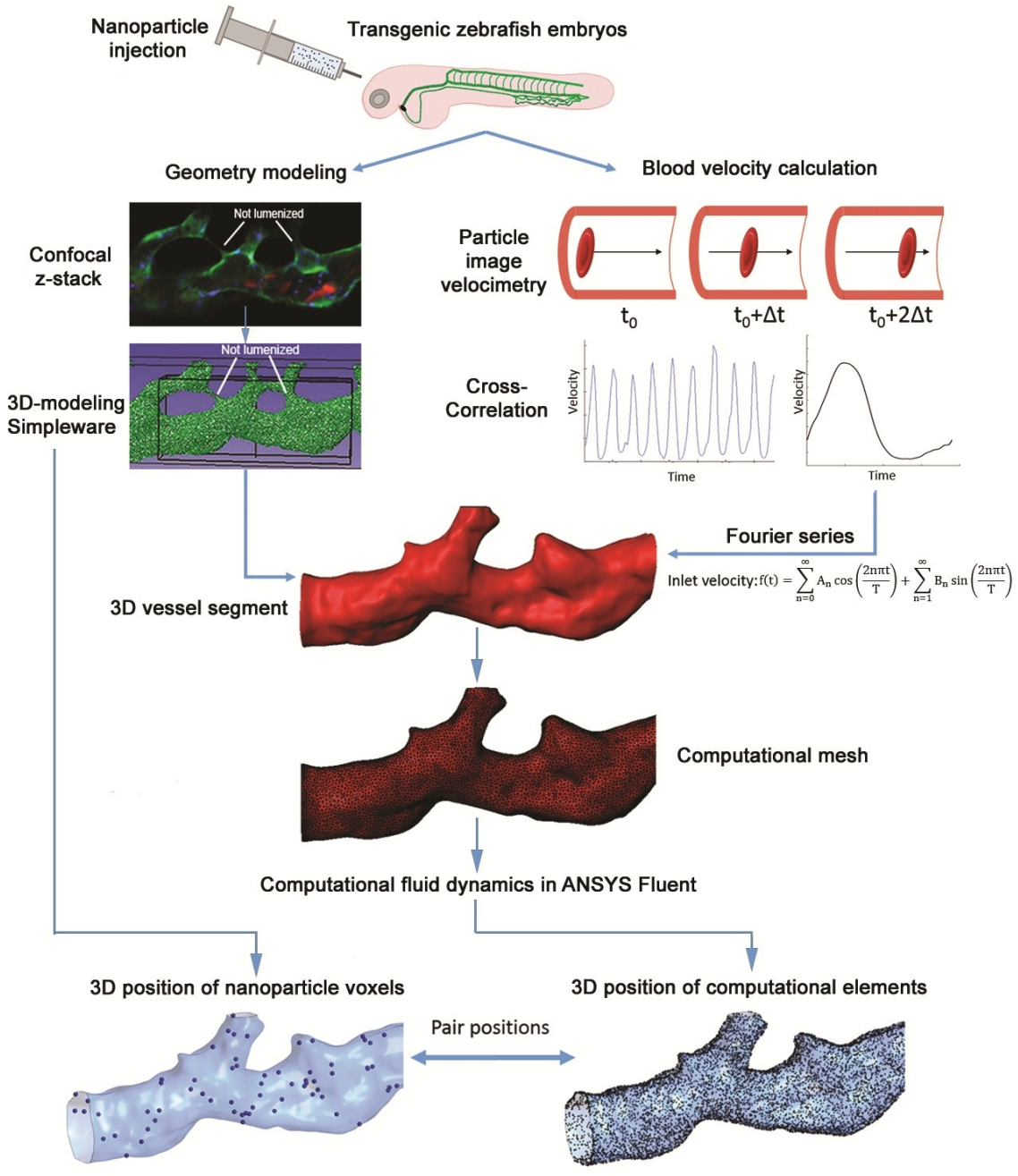


**S Figure 1.** Schematic of the *in vivo* evaluation of flow effects on nanoparticle localization. Details of the methodology are found in the Methods section of the main manuscript.

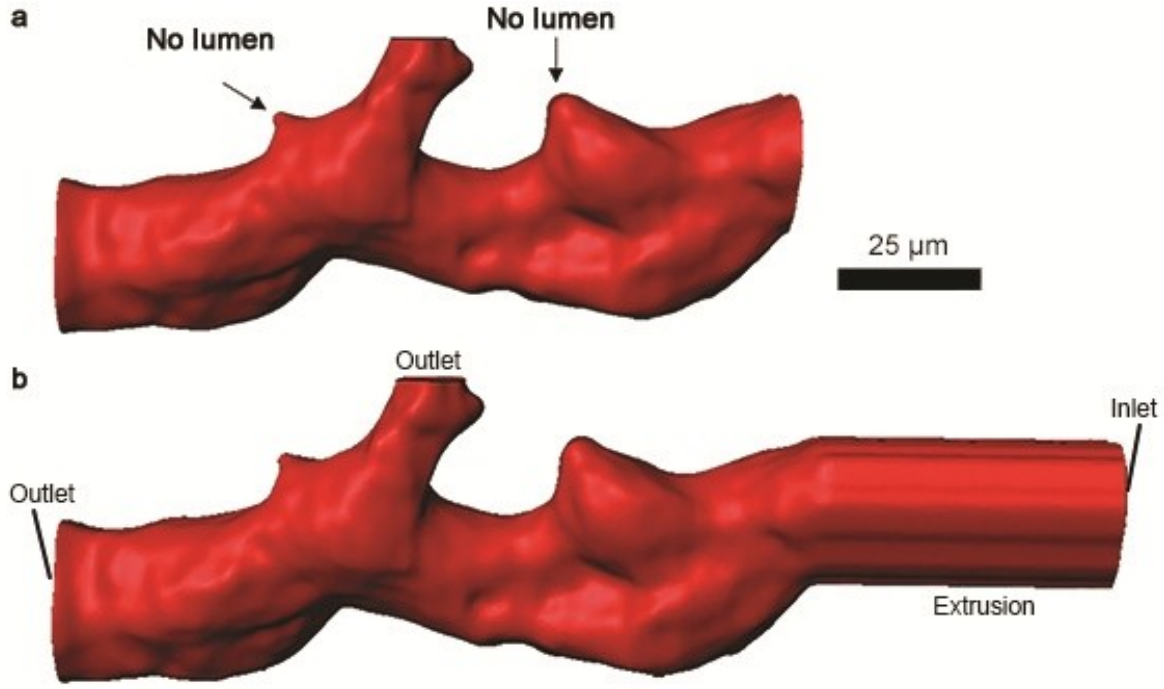


**S Figure 2.** 3D geometry of the zebrafish caudal vein. (a) Smoothed model of the vein segment outlined in the region of interest, black arrows show the vessels that were cropped and modelled as bumps since they were not fully formed and did not have flow in the luminal region. Black scale bar applies for c and d. (b) Model with the extruded inlet (2 diameters in length) to provide a path for the flow to develop before entering the region of interest.

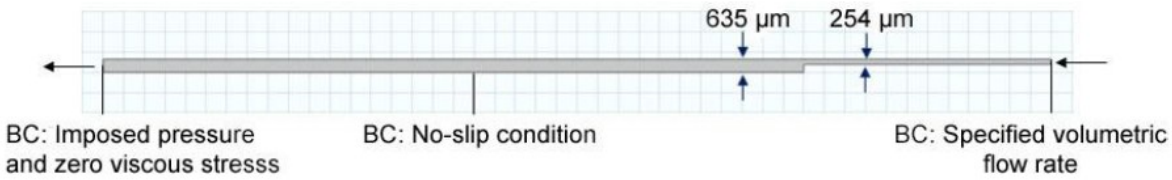


**S Figure 3.** Two-dimensional geometry of the sudden expansion flow chamber used to expose cultured human umbilical vein endothelial cells to flow and nanoparticles. Arrows show the direction of flow. Inlet was adjusted to flow rates that would generate shear stresses of 0.1, 0.2, and 0.8 Pa.

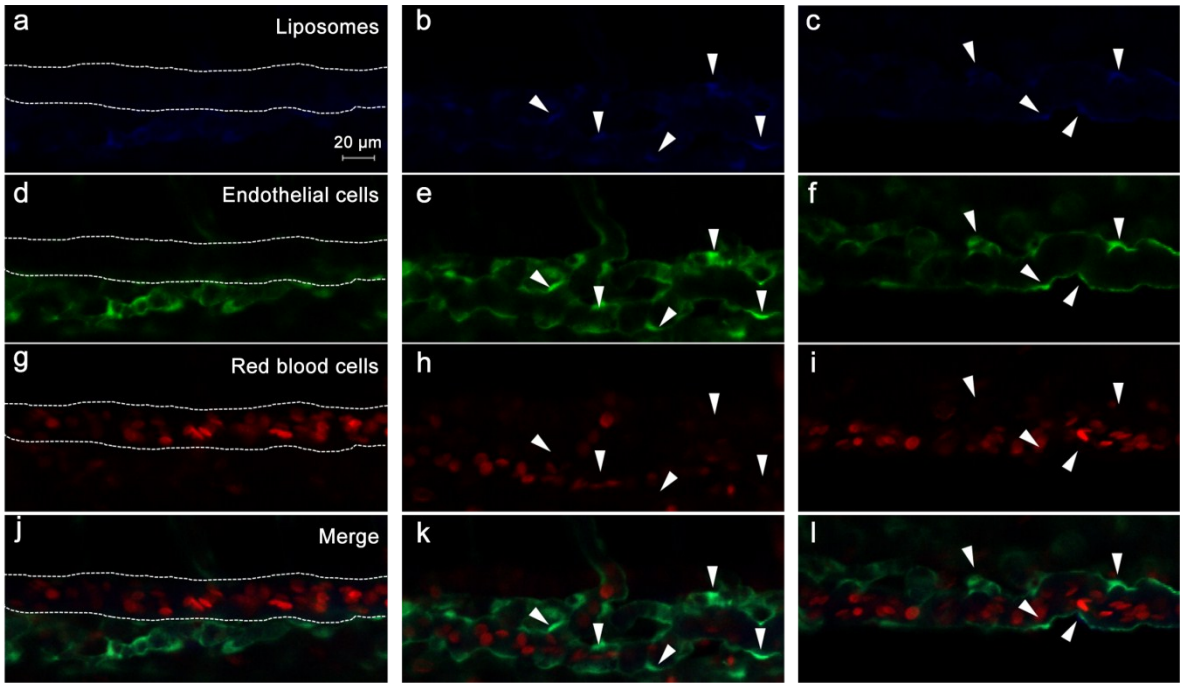


**S. Figure 4.** Liposome accumulation in the caudal region zebrafish embryo vasculature. Liposome accumulation in the (a) dorsal aorta (DA), (b) caudal venous plexus (CVP) encompassing the dorsal vein and capillaries, and (c) caudal ventral vein (VV). Endothelial cells expressing green fluorescent protein (d) DA, (e) CVP, (f) VV. Red blood cells expressing DsRed in the (g) DA, (h) CVP, (i) VV. Merge of channels for the (j) DA, (k) CVP, (l) VV. White dashed lines in the first column encompass the region of the DA, white arrows in last two columns denote regions where maximum liposome accumulation seems to occur. Blue signal from liposomes was enhanced for publication. Images are representative of a sample of three.

## Results

### *Nanoparticle characterization*

The hydrodynamic diameter of the polystyrene nanoparticles was 180.8 ± 1.2 nm based on number size measurements (201.9 ±2.5 nm based on intensity and 204.0 ± 2.2 nm based on volume measurements). Since nanoparticle surface charge greatly affects how they interact with the surrounding environment and also indicates colloidal stability, particle zeta potential was measured. Nanoparticles had a large negative surface charge (zeta potential= -41.7 ± 1.0 mV), suggesting they were colloidally stable. Negatively charged particles were selected to study flow effects on nanoparticle localization since they are not electrostatically attracted to the endothelial glycocalyx (that has a net negative charge) unlike cationic particles.[1] Additionally, the mean polydispersity index was 0.015 ± 0.011, indicating monodispersed nanoparticles.

## Methods

### *Nanoparticle size and zeta potential measurements*

Carboxylate-coated FluoSpheres (2% w/v, red fluorophore-loaded, 200 nm diameter polystyrene nanoparticles, Thermo Fisher Scientific, Waltham, MA) were diluted to nanomolar concentrations in ultrapure water and tested for mean size diameter, polydispersity index (PdI) and zeta-potential using Zetasizer Nano ZS (DTS 1060, Malvern Instruments Ltd., Worcestershire, UK) at 25°C. Measurements were conducted in triplicates and values were reported as mean ± standard deviation.

## *Computational fluid dynamics zebrafish embryo*

Simulation of transient flow was performed assuming blood plasma and red blood cell hemoglobin behave as Newtonian fluids since embryonic great vessel microcirculation is governed by rigid blood cells.[2] The material properties were obtained from values previously reported in other investigations for zebrafish embryo blood, the density was defined as 1025 kg/m$^3$ [3] and the dynamic viscosity was 3 cP.[3–5] Blood was considered incompressible and the wall was assumed to be rigid. The domain was discretized into 3,303,489 tetrahedral finite volume elements, 247,103 elements were at the wall. The fluid flow velocity at the inlet was defined as a Fourier series approximation for the waveform found *in vivo* simulated for one cardiac cycle (0.38 s). For outlet boundaries, the pressure was specified as 0 Pa. The simulation of the flow in the zebrafish vein segment solved Navier-Stokes and continuity equations using the finite volume method. Wall shear stress with ten contours and velocity streamline plots were obtained using CFD-Post.

Navier-Stokes equation:

$$\rho\left(\frac{\partial u}{\partial t} + u \cdot \nabla u\right) = -\nabla p + \nabla \cdot \left(\mu\left(\nabla u + (\nabla u)^T\right) - \frac{2}{3}\mu(\nabla \cdot u)I\right) + F$$

Where u is the fluid velocity, p is the pressure, ρ is the density, μ is the dynamic viscosity, and F represents the external forces applied to the fluid. The equation can be simplified since the Reynolds number is very small (Re<1), meaning the inertial forces are very small compared to viscous forces and can be neglected. Additionally, gravity is neglected and the divergence of the velocity is equal to zero since the fluid is incompressible. The simplified Navier-Stokes equation is:

$$0 = -\nabla p + \nabla \cdot \left(\mu\left(\nabla u + (\nabla u)^T\right)\right)$$

Continuity equation:

$$\frac{\partial \rho}{\partial t} + \nabla \cdot (\rho u) = 0$$

For incompressible flows the continuity equation yields:

$$\nabla \cdot u = 0$$

For the time-dependent study, the boundary condition for the inlet was defined using a 'User defined-function' or UDF in Fluent that allows the user to define the boundary condition as a profile described by the Fourier series approximation. The Courant number was used to determine the maximum time step size to ensure that the time step duration is less than the time for the velocity wave form to travel to adjacent mesh grid points. The Courant number can be expressed as:

$$C = \frac{u\Delta t}{\Delta x} \leq C_{max}$$

Where u is the magnitude of the velocity, Δt is the time step, and Δx is the length between grid points. $C_{max}$ is equal to 1 when a time-marching solver is used. In this case, the peak velocity of the waveform (315 µm/s) was used as the velocity magnitude, and Δx was the minimum length of a tetrahedral element in the mesh (0.146 µm). Using this expression, the time step was set to 0.000463s and the simulation was performed for 820 steps since the total cycle was of 0.38s. Convergence for each time step of the transient study was set by x,y,z residuals below 1e-4 and continuity convergence of 1e-3.

## *In vivo time-averaged wall shear stress calculation*

Wall shear stress (WSS) values for every point in the mesh of the vessel wall were exported from ANSYS Fluent at every time step. WSS for laminar flows is defined as the change in velocity gradient normal to the vessel wall.

$$WSS = \mu\frac{\partial u}{\partial n}$$

Where µ is the dynamic viscosity of blood, u is the flow velocity, and n is the height above the boundary.

To calculate the changes in WSS throughout the cardiac cycle, the time averaged wall shear stress (TAWSS) was calculated for every point in the vessel including every time step.

$$TAWSS = \frac{1}{T}\int_0^T |WSS|dt$$

Where T is the duration of one cardiac cycle for the zebrafish embryo, and dt is the time step.

## *Image analysis for In vitro nanoparticle quantification*

To evaluate the difference in nanoparticle accumulation in vitro, images were taken from static conditions (n=4) and flow exposed cells (n=3). For each experimental replicate, several images were quantified and averaged to obtain a representative quantification. The total number images analyzed per condition were: static:36; 0.1 Pa = 115 laminar, 63 disturbed; 0.2 Pa = 60 laminar, 48 disturbed; 0.8 Pa= 42 laminar and 36 disturbed.

## *Parallel plate flow chamber*

A parallel-plate flow chamber employed in these studies was similar to that used in previous studies by our laboratory[6–8] and modified to incorporate a step gasket to enable a sudden expansion recirculation region.[9–11] Two rectangular silicon gaskets with cut-outs to form a flow channel with a backwards facing step were sandwiched between a ported polycarbonate top plate and a cell-seeded glass slide. A glass field finder slide (Gurley Precision Instruments, Troy, NY) used for gasket alignment and distance measurements was placed

underneath the cell-seeded slide. The entire assembly was held together with hand-tightened clamps. The top gasket was 254 µm thick, $h_1$, and had a cut-out region of 1.25 cm width, $w$, by 4.59 cm length, while the bottom gasket formed the backward facing step and was 381 µm thick, $h_2$, with a cut-out region of 1.25 cm width and 3.4 cm length. The upstream flow path was 1.19 cm long and accommodated the entrance length for flow development prior to encountering the step. The entrance length for a rectangular channel was defined as:

$$L = 0.08HRe$$

where $H$ was the height of the chamber ($h_1 + h_2$) and $Re$ was the Reynolds number (21.0 for 0.1 Pa, 42.1 for 0.2 Pa, and 168 for 0.8 Pa). The Reynolds number was calculated for each flow rate as previously described for a similar flow chamber by:[11]

$$Re = \frac{2Q}{v(w + H)}$$

where $v$ is the kinematic viscosity (0.007964 cm$^2$/s), $Q$ is the volumetric flow rate (6.6 mL/min at 0.1 Pa, 13.2 mL/min at 0.2 Pa, and 52.8 mL/min at 0.8 Pa), and $w$ is the width of the chamber. Therefore, the flow entering the sudden expansion was considered fully developed at all values of shear stress used here. The expansion ratio ($H/h_1$) was 2.5.
Downstream of the expansion, fully-developed laminar flow was established and the wall shear stress, $\tau$, for the channel described by:

$$\tau = \frac{6Q\mu}{wH^2}$$

where µ is the fluid viscosity.

## *Computational fluid dynamics sudden expansion flow chamber*

A CFD model was constructed in a commercial CFD code COMSOL, 2012. In this CFD code, the Navier-Stokes equations are solved by using the finite element method. The domain with gap dimensions and boundary conditions (BC) is shown in supplementary Figure 4. The upstream and downstream gaps were taken to be long enough to provide well-developed flow within the upstream and downstream gaps before and after the step, respectively. Geometry was built in 2D using the exact measurements of the flow chamber. The material properties were obtained from the characterization of EGM2 cell culture media, the density was defined as 1 kg/m$^3$ and the dynamic viscosity at 37˚C was 0. 79464 cP. The domain was discretized into 569,744 triangular (mostly within the central parts of the domain) and quadrilateral (mostly near the boundaries) finite elements; the minimum and maximum sizes of the finite elements were equal to about 1.02 and 28.5 µm, respectively. At the inflow boundary, the liquid flow rate was imposed whereas at the outflow boundary, the pressure was specified with zero viscous stress. At the walls, the no-slip condition was applied. The simulation for the laminar incompressible flow present in the flow chamber was performed using the PARDISO direct solver. Recirculation areas were identified by plotting 250 velocity streamlines for each inflow condition.

*Computational fluid dynamics in vitro validation*

Based on studies by Truskey et al.[12] of a sudden expansion chamber and measurements of the recirculation zone observed using a phase contrast light microscope (Nikon Eclipse TE200, Japan) and microspheres (CaliBRITE 3, BD Biosciences, San Jose, CA), the linear distance from the step gasket was used to determine whether the ROI was exposed to disturbed flow or laminar flow. Additionally, velocity streamlines and WSS profiles were generated using CFD software Comsol Multiphysics, to determine the reattachment point and the flow recovery segment for each level of shear stress.

## References


1 S. Honary and F. Zahir, *Trop. J. Pharm. Res.*, 2013, **12**, 255-264
2 C.-Y. Chen, M. J. Patrick, P. Corti, W. Kowalski, B. L. Roman and K. Pekkan, *Biorheology*, 2011, **48**, 305–321.
3 A. Santhanakrishnan and L. A. Miller, *Cell Biochem. Biophys.*, 2011, **61**, 1–22.
4 H. Anton, S. Harlepp, C. Ramspacher, D. Wu, F. Monduc, S. Bhat, M. Liebling, C. Paoletti, G. Charvin, J. B. Freund and J. Vermot, *Dev. Camb. Engl.*, 2013, **140**, 4426–4434.
5 J. R. Hove, R. W. Köster, A. S. Forouhar, G. Acevedo-Bolton, S. E. Fraser and M. Gharib, *Nature*, 2003, **421**, 172–177.
6 K. D. Viegas, S. S. Dol, M. M. Salek, R. D. Shepherd, R. M. Martinuzzi and K. D. Rinker, *Biomed. Eng. Online*, 2011, **10**, 20.
7 R. D. Shepherd, S. M. Kos and K. D. Rinker, *Biorheology*, 2009, **46**, 529–538.
8 R. D. Shepherd, S. M. Kos and K. D. Rinker, *Am. J. Physiol. Heart Circ. Physiol.*, 2011, **301**, H98–H107.
9 J.-J. Chiu and S. Chien, *Physiol. Rev.*, 2011, **91**, 327–387.
10 G. A. Truskey, K. M. Barber, T. C. Robey, L. A. Olivier and M. P. Combs, *J. Biomech. Eng.*, 1995, **117**, 203–210.
11 V. Z. McKinney, K. D. Rinker and G. A. Truskey, *J. Biomech.*, 2006, **39**, 806–817.
12 G. A. Truskey, K. M. Barber, T. C. Robey, L. A. Olivier and M. P. Combs, *J. Biomech. Eng.*, 1995, **117**, 203–210.